Available online at www.sciencedirect.com

ScienceDirect

Journal of Magnesium and Alloys 12 (2024) 767–778

www.elsevier.com/locate/jma

Full Length Article

TiO_2@C catalyzed hydrogen storage performance of Mg-Ni-Y alloy with LPSO and ternary eutectic structure

Wenjie Song[a,b,*], Wenhao Ma[a], Shuai He[a], Wei Chen[b], Jianghua Shen[c], Dalin Sun[b], Qiuming Wei[d], Xuebin Yu[b,*]

[a] College of Mechanical and Electrical Engineering, Shaanxi University of Science and Technology, Xi'an, Shaanxi 710021, China
[b] Department of Materials Science, Fudan University, Shanghai 200438, China
[c] School of Aeronautics, Northwestern Polytechnical University, Xi'an, Shaanxi 710072, China
[d] Department of Mechanical Engineering & Engineering Science, the University of North Carolina at Charlotte, Charlotte, North Carolina 28223, United States of America

Received 7 December 2022; received in revised form 28 March 2023; accepted 26 April 2023
Available online 12 May 2023

Abstract

A designed $Mg_{88.7}Ni_{6.3}Y_5$ hydrogen storage alloy containing 14H type LPSO (long-period stacking ordered) and ternary eutectic structure was prepared by regulating the alloy composition and casting. The hydrogen storage performance of the alloy was improved by adding nano-flower-like TiO_2@C catalyst. The decomposition of the LPSO structure during hydrogenation led to the formation of plenty of nanocrystals which provided abundant interphase boundaries and activation sites. The nanoscale TiO_2@C catalyst was uniformly dispersed on the surface of alloy particles, and the "hydrogen overflow'' effect of TiO_2@C accelerated the dissociation and diffusion of hydrogen on the surface of the alloy particles. As a result, the *in-situ* endogenous nanocrystals of the LPSO structure decomposition and the externally added flower-like TiO_2@C catalyst uniformly dispersed on the surface of the nanoparticles played a synergistic catalytic role in improving the hydrogen storage performance of the Mg-based alloy. With the addition of the TiO_2@C catalyst, the beginning hydrogen desorption temperature was reduced to 200 °C. Furthermore, the saturated hydrogen absorption capacity of the sample was 5.32 wt.%, and it reached 4.25 wt.% H_2 in 1 min at 200 °C and 30 bar.

Keywords: Hydrogen storage; Mg; LPSO; TiO_2@C; Synergistic catalysis.

1. Introduction

The massive consumption of fossil fuels has led to global warming caused by carbon emissions. It is increasingly important to find economical and reliable clean energy to replace fossil fuels in daily life and industrial production. Hydrogen has been considered as a secondary energy source with great potential for its high energy density, environmental friendliness and renewability [1,2]. Hydrogen storage and transportation are the keys to the development of the hydrogen economy [3,4]. Magnesium (Mg) has been widely considered as an ideal large-scale hydrogen storage medium for its high hydrogen storage capacity, low price, and good reversibility. However, the quite slow kinetics and high temperature needed for pure Mg for this function restrict its application in hydrogen storage [5,6]. Alloying [7–9], nanocrystallization and adding catalysts [10–12] are the primary means to improve the hydrogen storage capacity of Mg-based hydrogen storage materials. However, these methods are often accompanied by the introduction of other elements, which leads to a decrease in the hydrogen storage capacity of magnesium-based hydrogen storage materials. As such, how to balance between ki-

* Corresponding authors.
E-mail addresses: songwenjie@sust.edu.cn (W. Song), yuxuebin@fudan.edu.cn (X. Yu).

https://doi.org/10.1016/j.jma.2023.04.002

netics and storage capacity has pose a key challenge in this area.

Alloying is an important strategy to concomitantly improve the hydrogen absorption and desorption kinetics, and to tailor the thermodynamics of Mg. Mg-based hydrogen storage alloys, especially the Mg-Ni-RE system, have greatly improved their hydrogen absorption and desorption properties due to the addition of transition metal elements (such as Ni) [13–16]. Zhang et al. [17] studied the effect of RE alloying on the hydrogen storage properties and reaction mechanisms of the $Mg_{90}Ce_5Sm_5$ ternary alloy. The alloy shows good isothermal hydrogen absorption kinetics because of the profuse high-angle boundaries between the LPSO phase and the matrix, and the short hydrogen diffusion paths and the low energy barrier inside the LPSO structure. Pan et al. [18] prepared Mg-Ni-Y alloys and obtained 14H type LPSO phase in the ternary eutectic region. The LPSO phase is activated and decomposed into a large number of fine and uniformly dispersed catalytic phases. In addition, nanoscale YH_2 and YH_3 phases are formed during hydrogenation. At the same time, the formed fine phase plays a catalytic role in promoting the hydrogen storage performance of the alloy.

The addition of catalyst can effectively improve the dissociation rate of hydrogen molecules on the surface of metals [19–22], and the penetration of hydrogen atoms from the surface into the metal [16,20,23]. Catalyst nanosizing can increase catalytic activity, but agglomeration of nanocatalysts on the alloy surface and detachment from the alloy can also lead to a reduction in catalytic efficiency. To improve catalytic efficiency, the dispersion, homogeneity of distribution and bonding of the catalyst to the substrate needs to be improved as much as possible. Zhang et al. [16] prepared La-Sm-Mg-Ni alloy with 5 wt.% TiO_2 and La_2O_3 catalysts respectively. The results show that the catalysts could improve the ball milling efficiency, activation performance, hydrogen absorption and desorption kinetics of the composite alloys. Zhang et al. [24] observed *in-situ* growth of MgH_2 nanoparticles in carbon materials by a simple chemical solid-state method, in which the laminar structure consisting of interconnected folds with a large specific surface area is most favorable for maintaining the high dispersion and nano-size of MgH_2 nanoparticles, resulting in better hydrogen absorption and desorption properties. In summary, the nano-TiO_2 catalyst has good catalytic effect but is prone to agglomeration. The decrease in catalytic efficiency caused by agglomeration can be effectively solved by homogeneously loading the catalyst onto the C-support material. The doping of transition metal elements combined with the addition of catalyst to modify the surface of alloy particles is expected to solve the thermodynamic and kinetic deficiencies of hydrogen absorption/desorption in Mg-based hydrogen storage materials.

In this work, an Mg-rich alloy, $Mg_{88.7}Ni_{6.3}Y_5$ was designed with high theoretical hydrogen storage capacity. The composition of the alloy was within the range for the formation of the LPSO structure. After high energy ball milling, the alloy particles were refined to nanoscale with a high specific surface area. The endogenous and external catalysts were both introduced into the alloy via *in-situ* reaction and external doping with TiO_2@C catalyst to improve the thermodynamic and kinetics of hydrogen absorption and desorption by combining multiphase eutectic structure and nanoscale refinement. This work should provide theoretical support for the research of synergistic catalysis of *in-situ* endogenous and externally added nano-catalysts.

2. Experimental

2.1. Materials preparation

To avoid oxidation of Mg, the $Mg_{88.7}Ni_{6.3}Y_5$ ternary alloy was prepared using a resistance furnace under the protection of a covering agent. The protective covering agent consisted of 44% $MgCl_2$, 44% KCl, 7% $BaCl_2$ and 5% CaF_2 (all in wt.%). The covering agent was melted at 973 K and then milled to powder after solidification. The covering agent power was sprinkled on the raw metal blocks before melting of the $Mg_{88.7}Ni_{6.3}Y_5$ alloy which was covered during the subsequent melting process to prevent the oxidation and violent burning of the magnesium alloy. The raw materials were master alloys of Mg-30Y (purity 99.9%), Mg-50Ni (purity 99%) and Y ingot (purity 98.7%). Nanoscale alloy powder was prepared by high-energy ball milling in a horizontal planetary mill at milling speed of 350 rpm for 31 h with a ball to material ratio of 20:1 in Ar atmosphere. The TiO_2@C was synthesized according to the Rev. [25]. The content of each element in the prepared nanomaterials is Ti 10.34%, O 23.60% and C 66.06% respectively. 1.0 wt.% of TiO_2@C nanoparticles were added into the alloy via milling for more 15 min, and the mass fraction of the active ingredient TiO_2 was calculated to be 0.524 wt.%. All operations were carried out in an argon atmosphere glove box to prevent oxidation.

2.2. Analysis and characterization

The phase composition before and after hydrogenation and dehydrogenation was analyzed by an X-ray diffractometer (RIGAKU, smart lab 9 kW) with Cu Kα radiation, with 2θ from 10° to 80°, scanning speed 5°/min with an applied voltage of 45 kV and current of 200 mA. The microstructure of the as-cast alloy was observed by SEM (FEI, Verios 460). Transmission electron microscopy (TEM) and corresponding elemental analysis were performed on FEI Tescan G3. The initial dehydrogenation temperature and thermodynamic performance of the samples were examined by DSC (SDT-Q600). The heating rates were 5, 10, 15 and 20 K/min, and the temperature ranged from room temperature to 500 °C. The activation and hydrogen storage properties of the as-cast alloys were measured by a Sievert's apparatus (Pressure Composition Temperature (PCT) Pro E&E). The samples were activated by three cycles of hydrogen absorption and desorption before hydrogen storage measurement. The initial hydrogen pressure was 30 bar and it was kept at 573 K for 10 h, and then dehydrogenation condition was vacuum during activation. The kinetic and thermodynamic measurements of the

samples were performed at 200, 250, 300, 325 and 350 °C, respectively.

3. Results and discussion

3.1. Phase composition

Fig. 1(a) shows the XRD results of ball-milled $Mg_{88.7}Ni_{6.3}Y_5$ and added with TiO_2@C alloys before hydrogenation. The main components of the ball-milled $Mg_{88.7}Ni_{6.3}Y_5$ sample were Mg and $Mg_{15}NiY$. In our preparatory work, the $Mg_{15}NiY$ was determined to be a 14H-type LPSO structure [13]. After adding the TiO_2@C catalyst, the diffraction peak intensity of the $Mg_{15}NiY$ and $MgNi_4Y$ phases decreased significantly, and the diffraction peak intensity and width of the Mg phase increased. The catalyst improved the ball milling efficiency and reduced the particle size of the alloy as a grinding aid. After adding the catalyst followed by ball milling for 15 min, the phase composition changed. Both samples contained Mg, Mg_2Ni and $Mg_{15}NiY$ phases. The difference was that the content of $Mg_{15}NiY$ decreased and the content of Mg increased after adding the catalyst and ball milling for 15 min. This might be because the grinding efficiency was improved with the catalyst TiO_2@C, and the particle size became smaller during the fifteen-minute ball milling. The original LPSO structure was further broken, and as such the proportion of pure Mg particles was further increased, leading to significant change in phase composition. Zhu et al. [26] reported a reduction in the phase content of the LPSO structure in XRD results after ball milling, but the lamellar structure of LPSO was still observed in bright-field TEM. The LPSO structure of this work was still present after ball milling. Fig. 1(b) shows the XRD results of hydrogenated ball-milled $Mg_{88.7}Ni_{6.3}Y_5$ with and without TiO_2@C catalyst. The results showed that the samples were mainly hydrogenated as MgH_2, Mg_2NiH_4, YH_2 and YH_3. The intensity of MgH_2 increased significantly with TiO_2@C, indicating that the addition of the catalyst was conducive to the formation of MgH_2 and thus increased the hydrogen storage capacity of the alloy. This was consistent with the increase in hydrogen absorption of the first platform in the subsequent pressure-composition-temperature (PCT) curve analysis.

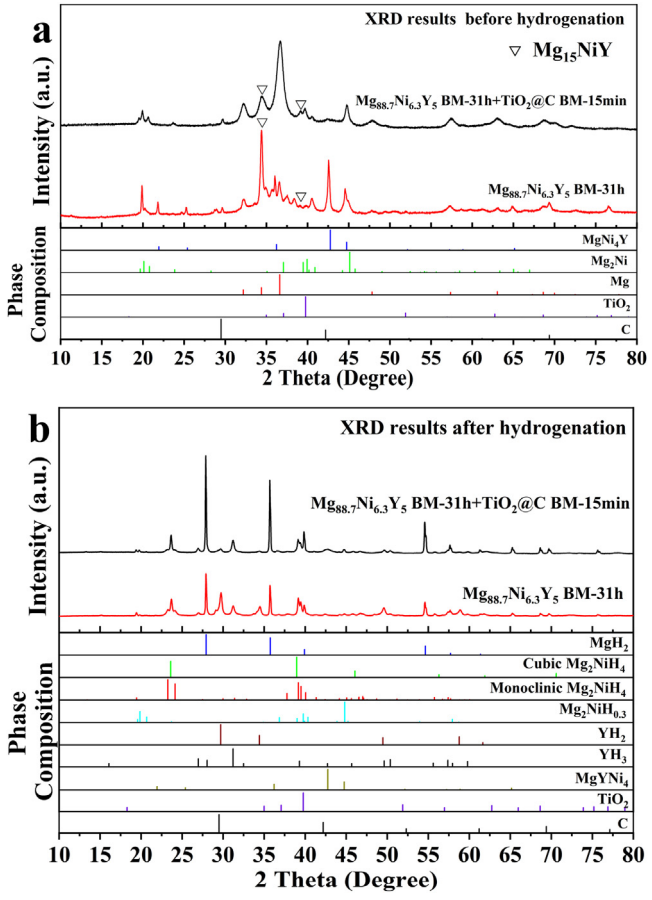

Fig. 1. XRD results of $Mg_{88.7}Ni_{6.3}Y_5$ as-cast alloy and catalyzed with TiO_2@C (a) before and (b) after hydrogenation.

3.2. Microstructure

Fig. 2 shows the SEM images of $Mg_{88.7}Ni_{6.3}Y_5$ as-cast alloy. There were four phases with different contrast and morphology, including $Mg_{15}NiY$ (LPSO), Mg, Mg_2Ni and $MgNi_4Y$. The phase fractions were calculated to be (vol.%) Mg (30.98%), $Mg_{15}NiY$ (62.75%), Mg_2Ni (4.49%) and $MgNi_4Y$ (0.2%). The Mg_2Ni+Mg+$Mg_{15}NiY$ ternary eutectic microstructure with alternating layers of multiphases was observed in the as-cast alloy. The alloy $Mg_{88.7}Ni_{6.3}Y_5$ consisted of a large number of dark-gray flakes $Mg_{15}NiY$ (LPSO) and dark phase Mg. The composition corresponding to the LPSO structure had a range [27], and the designed alloy $Mg_{88.7}Ni_{6.3}Y_5$ was within this range. The acicular light gray flakes in the quadrilateral marking area were Mg_2Ni, with a width of about 5 μm and a length of about 60 μm. A small number of low-contrast polygon blocks of $MgNi_4Y$ were seen from the closed-up view in Fig. 2(b). During solidification, the $MgNi_4Y$ precipitated out first for its highest melting point. In this process, the content of Ni and Y in the residual liquid decreased, and Mg, $Mg_{15}NiY$ precipitated out. The Mg formed an irregular lamellar structure and increased the interface area. The $Mg_{15}NiY$ formed a wide skeleton with a width of ca. 20 μm. With further cooling, Mg, Ni and Y in the residual liquid underwent a ternary eutectic reaction to form a fine needle-like microstructure with Mg, Mg_2Ni and $Mg_{15}NiY$. The needle-like structure of 1∼3 μm wide and 50∼60 μm long had a large number of phase boundaries, which provided rich diffusion channels for hydrogen atoms and shortened the diffusion distance of hydrogen atoms.

Fig. 3 shows TEM images of ball-milled $Mg_{88.7}Ni_{6.3}Y_5$ alloy, TiO_2@C catalyst and $Mg_{88.7}Ni_{6.3}Y_5$ catalyzed with TiO_2@C before and after hydrogenation. Fig. 3(a) and (b) suggested the ball-milled $Mg_{88.7}Ni_{6.3}Y_5$ reached nanoscale size before hydrogenation. The Mg&Mg_2Ni phases were confirmed by selected area electron diffraction (SAED) insert in Fig. 3(b). The continuous diffraction rings also indicated the very fine grains of the ball-milled $Mg_{88.7}Ni_{6.3}Y_5$ alloy.

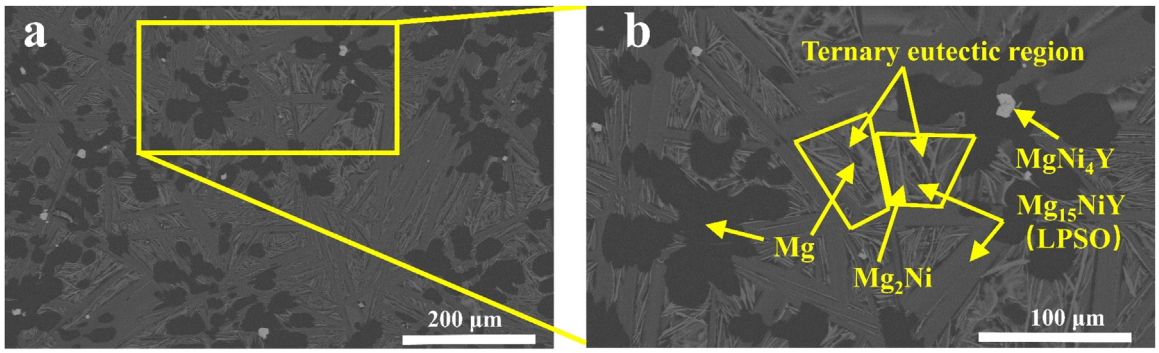

Fig. 2. SEM images of the $Mg_{88.7}Ni_{6.3}Y_5$ as-cast alloy; (a) SEM 500 X image and (b) typical local features in (a).

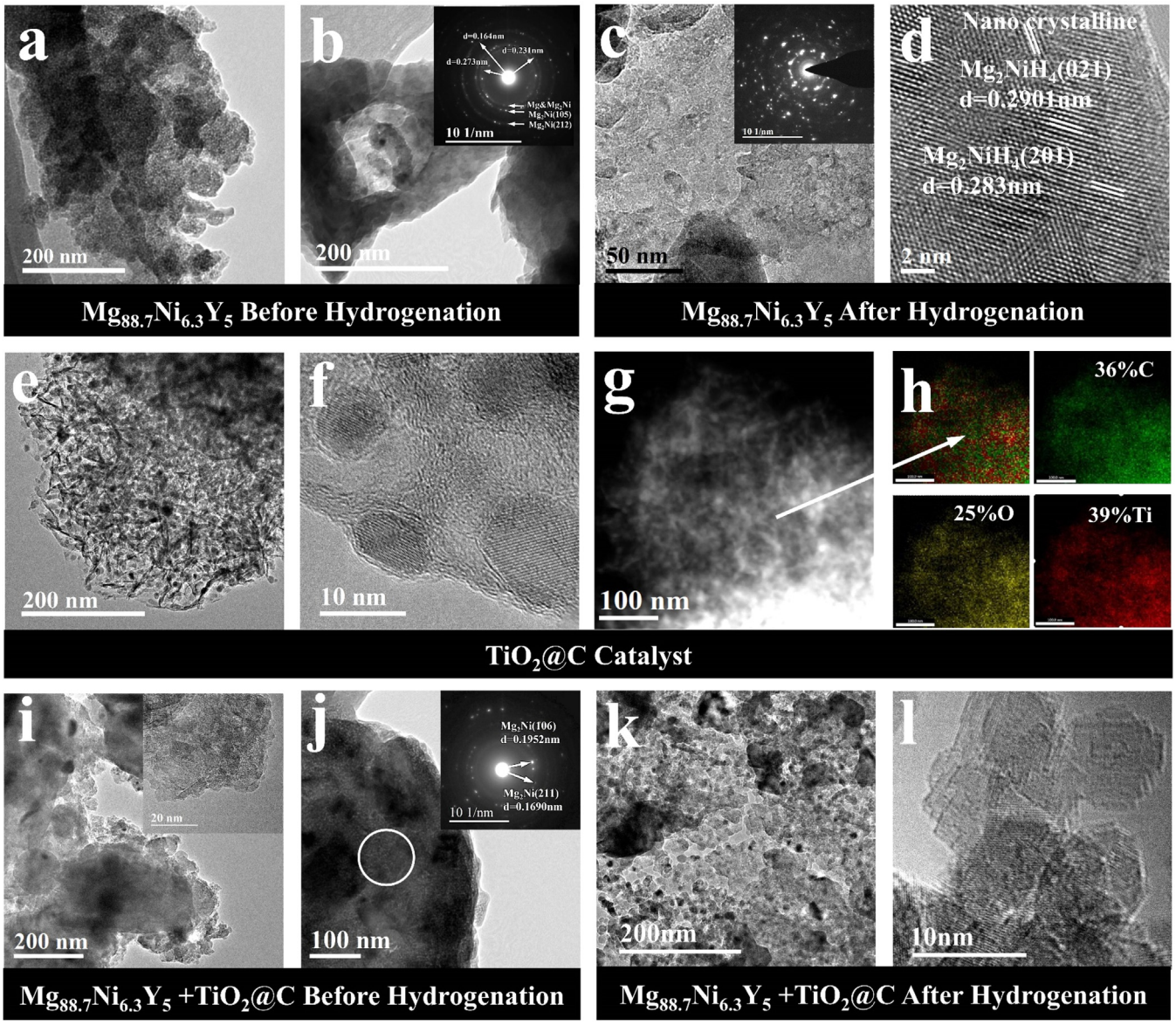

Fig. 3. TEM of the ball-milled $Mg_{88.7}Ni_{6.3}Y_5$ alloy, TiO_2@C catalyst and $Mg_{88.7}Ni_{6.3}Y_5$ alloy with TiO_2@C catalyst. (a) and (b) bright field images of ball-milled $Mg_{88.7}Ni_{6.3}Y_5$ alloy before hydrogenation; (c) microstructure and SAED of ball-milled $Mg_{88.7}Ni_{6.3}Y_5$ after hydrogenation; (d) HRTEM of $Mg_{88.7}Ni_{6.3}Y_5$ after hydrogenation; (e, f) microstructure and HRTEM of TiO_2@C catalyst; (g, h) EDS mappings of TiO_2@C catalyst; (i, j) microstructure and SAED of $Mg_{88.7}Ni_{6.3}Y_5$ with TiO_2@C catalyst before hydrogenation; (k, l) microstructure of $Mg_{88.7}Ni_{6.3}Y_5$ with TiO_2@C catalyst after hydrogenation.

Fig. 3(c) and (d) show the bright-field TEM images, the SAED and high-resolution TEM (HRTEM) image of ball-milled $Mg_{88.7}Ni_{6.3}Y_5$ alloy after hydrogenation. The TEM images along with the SAED showed that the hydrogenated $Mg_{88.7}Ni_{6.3}Y_5$ alloy was nanocrystalline (Fig. 3(c)). This was confirmed to be the Mg_2NiH_4 via HRTEM of Fig. 3(d). The Mg_2NiH_4 was the saturated hydrogenation product of Mg_2Ni. Tran [28] observed the hydrogen absorption and desorption of bulk Mg_2Ni using *in-situ* high-pressure TEM. A large number of cracks and dislocations were found during the hydrogen absorption and desorption processes. Repeated expansion and contraction of the lattice resulted in severe plastic deformation, which provided a large number of high-density layer faults. It provided a path for the diffusion of hydrogen atoms and reduced the nucleation barrier of Mg_2NiH_x ($x = 0\sim0.3$). The kinetics of hydrogenation was obviously improved.

Fig. 3(e-h) show the microstructure, HRTEM and energy dispersion spectrometry (EDS) mapping of the TiO_2@C catalyst. The TiO_2@C catalyst exhibited flower-like structure as shown in Fig. 3(e). The TiO_2 particles were about 8∼10 nm. These TiO_2 particles were homogeneously distributed on the surface of the low dimensional nanocarbon material (Fig. 3(e) and EDS mappings in Fig. 3(g, h)). The low-dimensional nanocarbon with a large specific surface area prevented the agglomeration of the nano-TiO_2 particles. In addition, it assisted the dissociation of hydrogen molecules on the surface of the alloy [20,29,30].

To confirm the distribution of the TiO_2@C catalyst on the surface of the sample, the sample doped with the flower-like TiO_2@C catalyst was also characterized by TEM. Fig. 3(i) and (j) show bright field TEM images and the SAED of ball-milled $Mg_{88.7}Ni_{6.3}Y_5$+TiO_2@C before hydrogenation. The particle size of $Mg_{88.7}Ni_{6.3}Y_5$+TiO_2@C was nanoscale before hydrogenation. The TiO_2@C catalyst was uniformly dispersed on the surface of the nanoparticles after ball milling for 15 min. The catalyst acted as the activation sites for hydrogen absorption and desorption, providing more diffusion channels for hydrogen atoms [31,32]. The addition of TiO_2@C catalyst refined the alloy particles by improving the milling efficiency as a ball milling auxiliary. It improved the hydrogen absorption and desorption kinetics of the sample by facilitating the rapid diffusion of hydrogen into the alloy particles. In the SAED inset of Fig. 3(j), the continuous diffraction rings were indexed to be of Mg_2Ni. Detailed analysis showed that the ball-milled samples contained a large amount of Mg_2Ni nanocrystalline phase.

The TEM images of the $Mg_{88.7}Ni_{6.3}Y_5$+TiO_2@C after hydrogenation were shown in Fig. 3(k, l). Nanometer hydrides appeared in the hydrogenated sample. Combined with XRD before and after hydrogenation, the Mg_2NiH_x ($x = 0.3\sim4$), YH_y ($y = 2, 3$) phases were confirmed to have formed from Mg_2Ni and $Mg_{15}NiY$ during hydrogenation. The $Mg_{15}NiY$ was transformed into 10∼30 nm MgH_2, Mg_2NiH_x ($x = 0.3\sim4$) and YH_y ($y = 2, 3$) during hydrogenation. The Mg_2NiH_x ($x = 0.3\sim4$) and YH_y ($y = 2, 3$) catalyzed the formation and decomposition of the MgH_2 phase. The *in-situ* formed Mg_2NiH_x ($x = 0.\ 3\sim4$) and YH_y ($y = 2, 3$) in

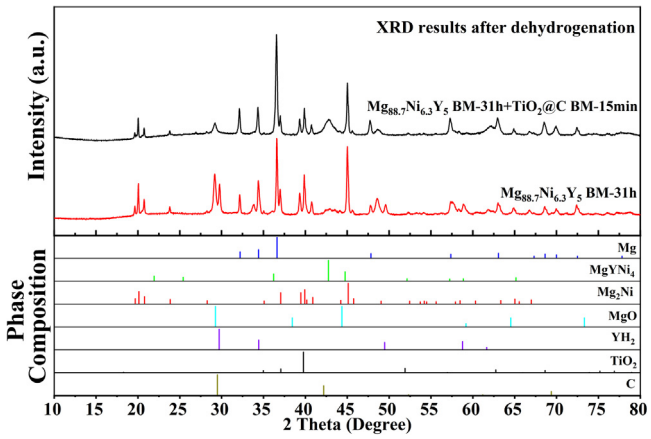

Fig. 4. XRD results of dehydrogenated $Mg_{88.7}Ni_{6.3}Y_5$ and TiO_2@C catalytic alloy.

LPSO showed catalytic activity. The TiO_2@C had a hydrogen overflow effect. First, the electronegativity of Ti is 1.54, which is between Mg (1.2) and H (2.1). The polyvalent Ti ions are more easily to gain electrons than Mg^{2+}, and more likely to lose electrons than H^-, which weakened the Mg-H bond. Moreover, the nanoscale TiO_2@C had a large number of contact sites with the alloy surface. These interfaces provided a large number of active centers for the valence state conversion between Ti, H and Mg ions. After hydrogenating several times, the multi-valence Ti-based catalysts were uniformly distributed on the surface of the alloy [33]. The TiO_2@C accelerated the absorption and desorption process of hydrogen. The multi-valent Ti-based catalyst acted as a carrier to assist the electron transfer between Mg and H, improving the kinetics of hydrogen absorption and desorption. The TiO_2@C catalyst and the *in-situ* nano-hydrides in LPSO improved synergistically the hydrogen absorption and dehydrogenation of the alloy.

Fig. 4 shows the XRD results of the dehydrogenated $Mg_{88.7}Ni_{6.3}Y_5$ and TiO_2@C catalyzed alloy. Compared with the XRD results of the ball-milled $Mg_{88.7}Ni_{6.3}Y_5$ alloy before hydrogenation (Fig. 1), the contents of Mg, Mg_2Ni and YH_2 increased significantly upon dehydrogenation. The phase of $Mg_{15}NiY$ could not be detected at all, indicating that it was converted to Mg, Mg_2Ni and YH_2 during the hydrogenation and dehydrogenation processes.

3.3. Hydrogen absorption and desorption kinetics

Fig. 5 shows the hydrogen absorption kinetics curves of $Mg_{88.7}Ni_{6.3}Y_5$ and the TiO_2@C catalyzed alloy. The LPSO structure of the $Mg_{88.7}Ni_{6.3}Y_5$ alloy had a great influence on the relationship between hydrogen absorption rate and temperature. The $Mg_{88.7}Ni_{6.3}Y_5$ could absorb about 4.4 wt.% hydrogen above 300 °C under 30 bar But the capacity decreased to 4.1 wt.% at 250 °C and 3.5 wt.% at 200 °C as shown in Fig. 5(a). The hydrogen absorption capacity of the alloy was increased to 5.32 wt.% with the addition of TiO_2@C catalyst (Fig. 5(b)). It is worth noting that the hydrogen absorption

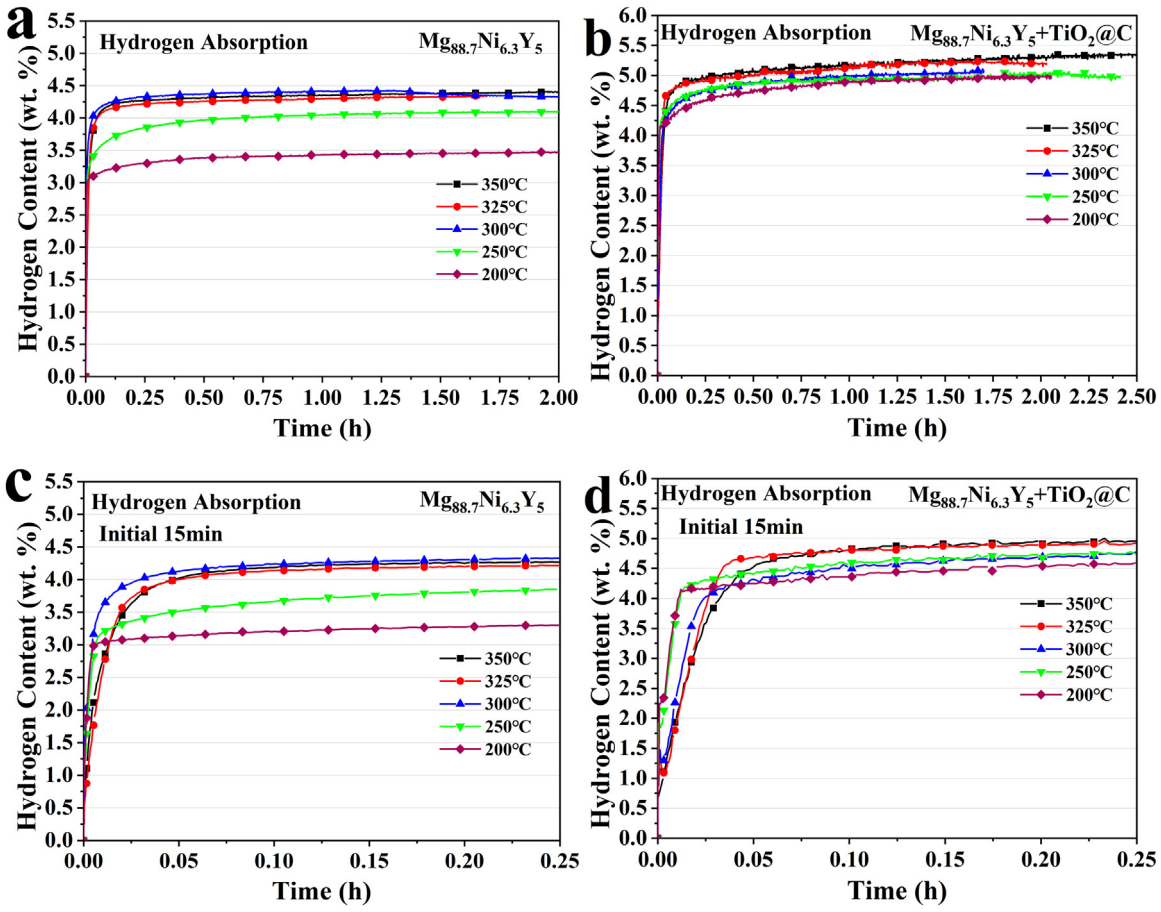

Fig. 5. Hydrogen absorption kinetics curves. (a) $Mg_{88.7}Ni_{6.3}Y_5$; (b) $Mg_{88.7}Ni_{6.3}Y_5$+TiO_2@C; (c) initial 15 min hydrogen absorption kinetics curves of $Mg_{88.7}Ni_{6.3}Y_5$; (d) initial 15 min hydrogen absorption kinetics curves of $Mg_{88.7}Ni_{6.3}Y_5$+TiO_2@C.

rate and capacity were improved at all temperatures, especially at low temperatures after adding the TiO_2@C catalyst. The hydrogen absorption capacity was insensitive to hydrogenation temperature above 200 °C. The hydrogen absorption capacity of the alloy powder could reach more than 5 wt.% even at 200 °C. It then transpires that the TiO_2@C-catalyzed $Mg_{88.7}Ni_{6.3}Y_5$ alloy could work at low temperatures for hydrogen absorption without affecting hydrogen absorption capacity.

Fig. 5(c) and (d) show the first initial 15 min hydrogen absorption kinetics curves of the two samples. Both the original $Mg_{88.7}Ni_{6.3}Y_5$ and the TiO_2@C catalyzed alloy powders demonstrated a fast rate and low temperature of hydrogen absorption in the initial 15 min. Both alloys could absorb approximately 85% of the corresponding saturated hydrogen absorption capacity in 2 min under 30 bar at 350, 325, 300, 250 and 200 °C. They exhibited faster hydrogen absorption rates at lower temperatures for the temperatures examined. This phenomenon was repeated in this work. It may be explained that lower temperature was beneficial to the exothermic reaction of hydrogenation and the increase of hydrogen absorption rate. With the addition of catalyst, the time to absorb 4 wt.% hydrogen was shortened to 0.5 min at 200 °C but was 1 min at 350 °C. Further analysis is needed to determine whether this is related to the presence of the LPSO structure in the alloy. However, the saturated hydrogen storage capacity was still directly proportional to temperature and pressure. Higher temperature and pressure were beneficial to promote the hydrogen absorption. Furthermore, the catalyst promoted the hydrogen absorption. The saturated hydrogen absorption capacity of the TiO_2@C catalyzed alloy powder was higher than that of the original $Mg_{88.7}Ni_{6.3}Y_5$ alloy.

Fig. 6 shows the dehydrogenation kinetics curve of $Mg_{88.7}Ni_{6.3}Y_5$ and TiO_2@C catalytic alloy. Both samples showed relatively high hydrogen desorption rates and capacities above 250 °C. The $Mg_{88.7}Ni_{6.3}Y_5$ alloy reached hydrogen desorption equilibrium in 30 min at all temperatures in this work. The dehydrogenation curves showed that the hydrogen desorption rate and capacity of TiO_2@C catalyzed alloy were higher than those of the original $Mg_{88.7}Ni_{6.3}Y_5$ alloy. The addition of TiO_2@C catalyst rendered it easier to approach the theoretical reversible hydrogen storage capacity under the experimental conditions for the $Mg_{88.7}Ni_{6.3}Y_5$ alloy. The hydrogenated TiO_2@C catalyzed $Mg_{88.7}Ni_{6.3}Y_5$ alloy desorbed 5.3 wt.% hydrogen in 3 min at 350 °C and 4.75 wt.% in 15 min at 250 °C. It was more than 1 wt.% hy-

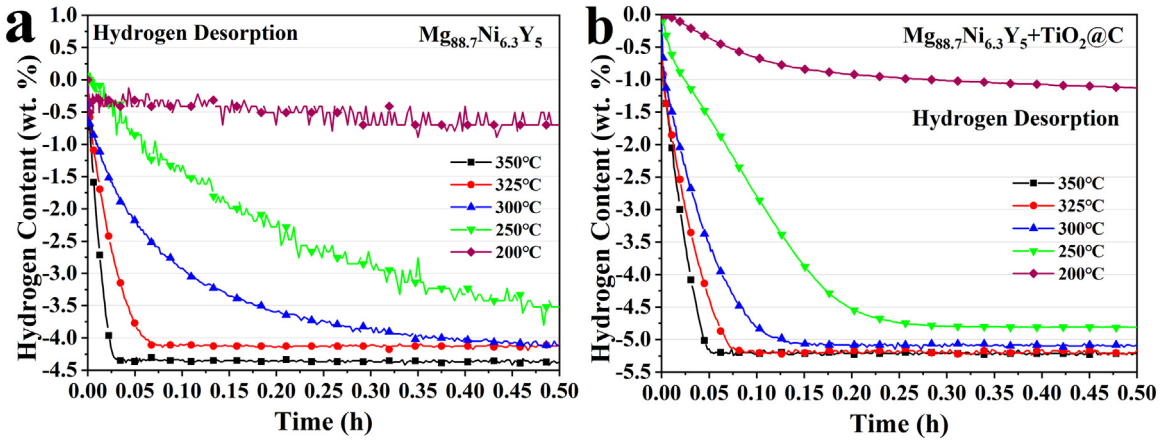

Fig. 6. Hydrogen desorption kinetics curves of (a) $Mg_{88.7}Ni_{6.3}Y_5$ and (b) $Mg_{88.7}Ni_{6.3}Y_5$+TiO_2@C.

drogen desorption content of the TiO_2@C catalyzed alloy at 200 °C. The TiO_2@C catalyst significantly improved the hydrogen absorption and dehydrogenation capacity and kinetics of $Mg_{88.7}Ni_{6.3}Y_5$ alloy, especially at low temperatures.

3.4. Hydrogen absorption and desorption thermodynamics

Fig. 7 shows the hydrogen absorption thermodynamics curves of the $Mg_{88.7}Ni_{6.3}Y_5$ and TiO_2@C catalyzed alloy. The TiO_2@C catalyst increased the hydrogen absorption thermodynamics plateau pressure and capacity significantly at 350 °C. With the addition of TiO_2@C catalyst, the plateau pressure increased by 2.5–3.0 bar for the first plateau and 5 bar for the second plateau. The hydrogen absorption capacity of the first hydrogen absorption plateau increased by 0.5 wt.% after adding TiO_2@C catalyst, while the second hydrogen absorption plateau did not change significantly. The first plateau was related to the hydrogen absorption of Mg. The hydrogen absorption capacity in the first plateau might be explained that the Mg phase could absorb hydrogen more completely in the sample after adding the catalyst. This was consistent with the XRD result of the appearance of MgH_2 after adding the TiO_2@C catalyst which accelerated the diffusion and transfer of hydrogen atoms through the "hydrogen overflow'' effect, avoiding the formation of the hydrogenation layer that adversely affected subsequent hydrogen absorption reactions [34]. On the other hand, the catalyst increased the plateau pressure for hydrogen absorption. In a certain range, the H_2 pressure was positively related to the amount of hydrogen absorbed by the sample. The high platform was mainly related to the Mg_2Ni/Mg_2NiH_4 phases. The corresponding hydrogen absorption thermodynamics of the Mg_2Ni phase was significantly improved in the $Mg_{88.7}Ni_{6.3}Y_5$ and TiO_2@C catalytic alloy. The corresponding hydrogen absorption thermodynamics of the Mg_2Ni phase was significantly improved in the $Mg_{88.7}Ni_{6.3}Y_5$ and TiO_2@C catalytic alloy. The formation enthalpy of Mg_2NiH_4 was reduced to −41.13 kJ/mol in the $Mg_{88.7}Ni_{6.3}Y_5$ alloy from −64.5 kJ/mol of regular Mg_2NiH_4. However, the addition of TiO_2@C did not significantly improve the thermodynamic properties of the material during hydrogen absorption.

Fig. 8 shows the hydrogen desorption thermodynamics curves of the $Mg_{88.7}Ni_{6.3}Y_5$ and TiO_2@C catalytic alloy. There was an obvious hysteresis effect of the hydrogen absorption and desorption thermodynamics. The platform pressures of the hydrogen desorption thermodynamics capacity were lower than those of hydrogen absorption thermodynamics curves as shown in Fig. 7(a) and (b). The plateau pressure of hydrogen desorption is 0.12 bar at 200 °C, and neither could desorb hydrogen completely for the low pressure during the hydrogen desorption process. When the pressure decreased to 0.8 bar, the hydrogen desorption stopped. The two inclined platforms in the dehydrogenation PCT curves illustrated that the hydrogen desorption process was the synergetic dehydrogenation of multiphases. Figs. 8(c) and (d) show the calculations of the Van't Hoff equation for hydrogen desorption before and after the addition of catalyst to the sample. Since the MgH_2−Mg system could not release hydrogen at 200 °C, the low plateau curve was only taken at four points for calculation. With the addition of TiO_2@C, the hydrogen desorption platform pressures were increased, and the enthalpy of hydrogen desorption of Mg was reduced by 7∼8 kJ/mol.

Fig. 9(a) shows the DSC curves of the $Mg_{88.7}Ni_{6.3}Y_5$ hydrogenated alloy samples at different heating rates. Two endothermic peaks appeared in the reaction process corresponding to the two platforms in the PCT curves. Combined with XRD analysis, the dehydrogenation phases were mainly Mg_2NiH_4, MgH_2, $Mg_2NiH_{0.3}$ and YH_3. In the Mg-Ni-Y system, the first heat absorption peak corresponded to the hydrogen release phases of mainly Mg_2NiH_4 and YH_3. The second peak was from dehydrogenation of MgH_2. In this work, the dehydrogenation starting temperature of the sample without catalyst was 460.78 K (187.63 °C) at a heating rate of 5 K/min. The first endothermic peak was at 488.91 K and the second one was 611.80 K. The first and second endothermic peaks were lower than those of the Mg_2NiH_4 and MgH_2, respectively. As such, the dehydrogenation temperature was reduced by the addition of Ni and Y.

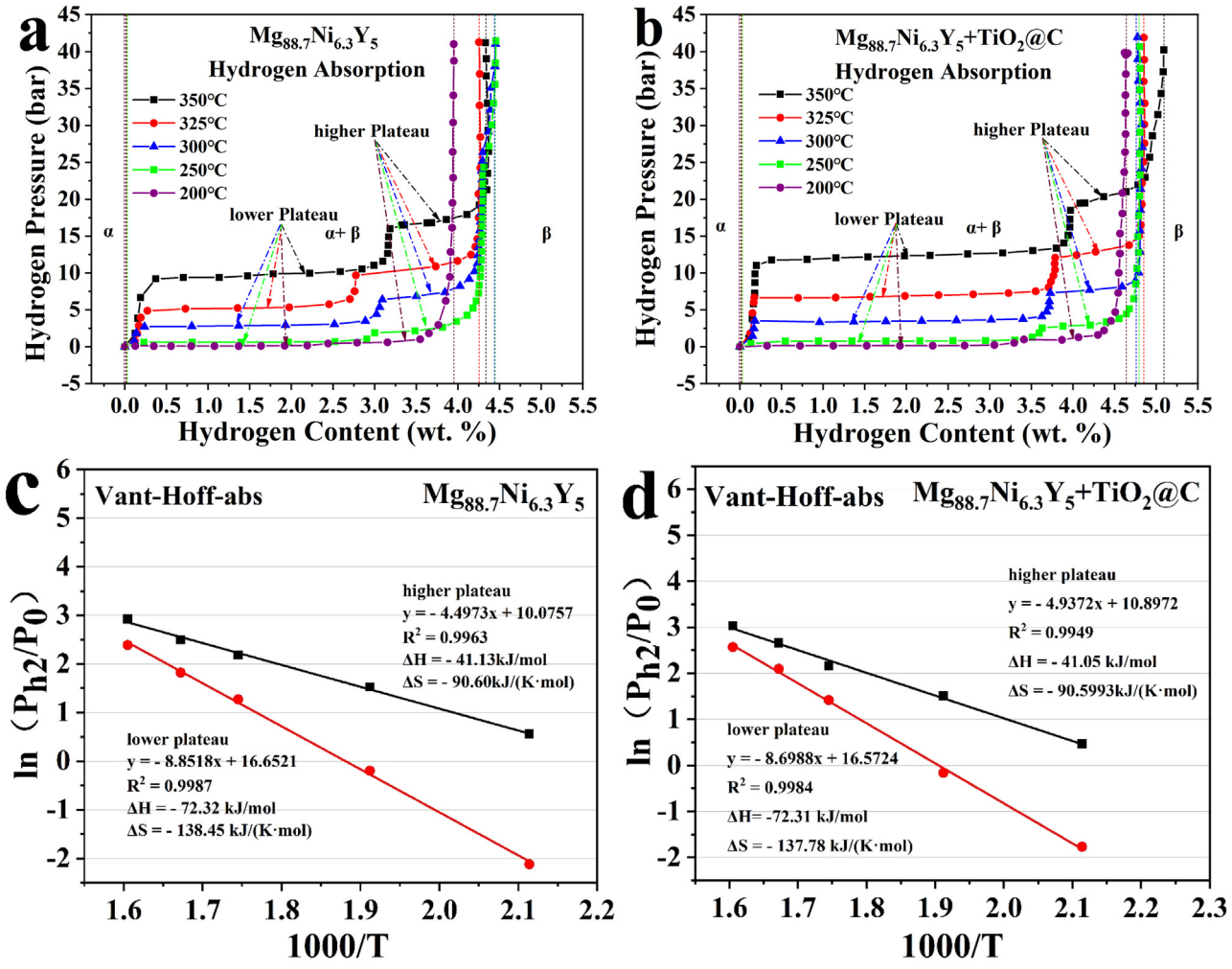

Fig. 7. Hydrogen absorption PCT and the Vant Hoff curves (a) $Mg_{88.7}Ni_{6.3}Y_5$; (b) $Mg_{88.7}Ni_{6.3}Y_5$+TiO_2@C; (c) $Mg_{88.7}Ni_{6.3}Y_5$ Vant-Hoff absorption curves; (d) $Mg_{88.7}Ni_{6.3}Y_5$+TiO_2@C Vant-Hoff absorption curves.

The dehydrogenation activation energies of the hydrides were calculated using the Kissinger equation. The Kissinger curves for the samples before adding catalyst were shown in Fig. 9(b). The dehydrogenation activation energy was 141.02 kJ/mol for MgH_2 and 91.47 kJ/mol for Mg_2NiH_4. Fig. 9(c) shows the DSC curves for the samples of $Mg_{88.7}Ni_{6.3}Y_5$ with TiO_2@C at different heating rates. The starting endothermic temperature with catalyst was 464.9 K (191.75 °C). The temperature range is 499.87 K of the first peak at a heating rate of 5 K/min, to 607.33 K of the second peak. There was no significant difference compared to the sample without the catalyst, indicating that the TiO_2@C catalyst did not continue to lower the starting endothermic temperature with the temperature of the peak. But the Kissinger curves in Fig. 9(d) show that the activation energy of dehydrogenation decreased to 85.93 kJ/mol for MgH_2 and 78.32 kJ/mol for Mg_2NiH_4 after the addition of the catalyst, indicating that the hydrogen desorption reaction was more likely to occur after the addition of the catalyst.

Tables 1 and 2 show the initial and peak temperatures of the heat absorption peaks with and without catalyst, respectively. The data in the two tables showed the initial dehydrogenation and peak temperatures of the first peak increased slightly after the addition of catalyst, while the initial dehydrogenation temperature of the second peak decreased and the peak temperature increased slightly. Such results were reproduced in this work. This might be because of the introduction of a small amount of oxide which raised the decomposition temperature of Mg_2NiH_4, though such oxide might have a significant catalytic effect on the decomposition of MgH_2. Since MgH_2 was the predominant hydride in the sample, corresponding to a low plateau that accounted for 80% of the total hydrogen uptake, the addition of the catalyst improved the overall thermodynamic properties of the sample.

3.5. Hydrogen absorption and desorption mechanism

The previous examination indicated that TiO_2@C was uniformly dispersed and flocculent on the surface of the alloy, with a large specific surface area. The hydrogen molecules diffused on the pure Mg surface and quickly formed a dense hydrogenation layer [35]. After full contact with the fully ac-

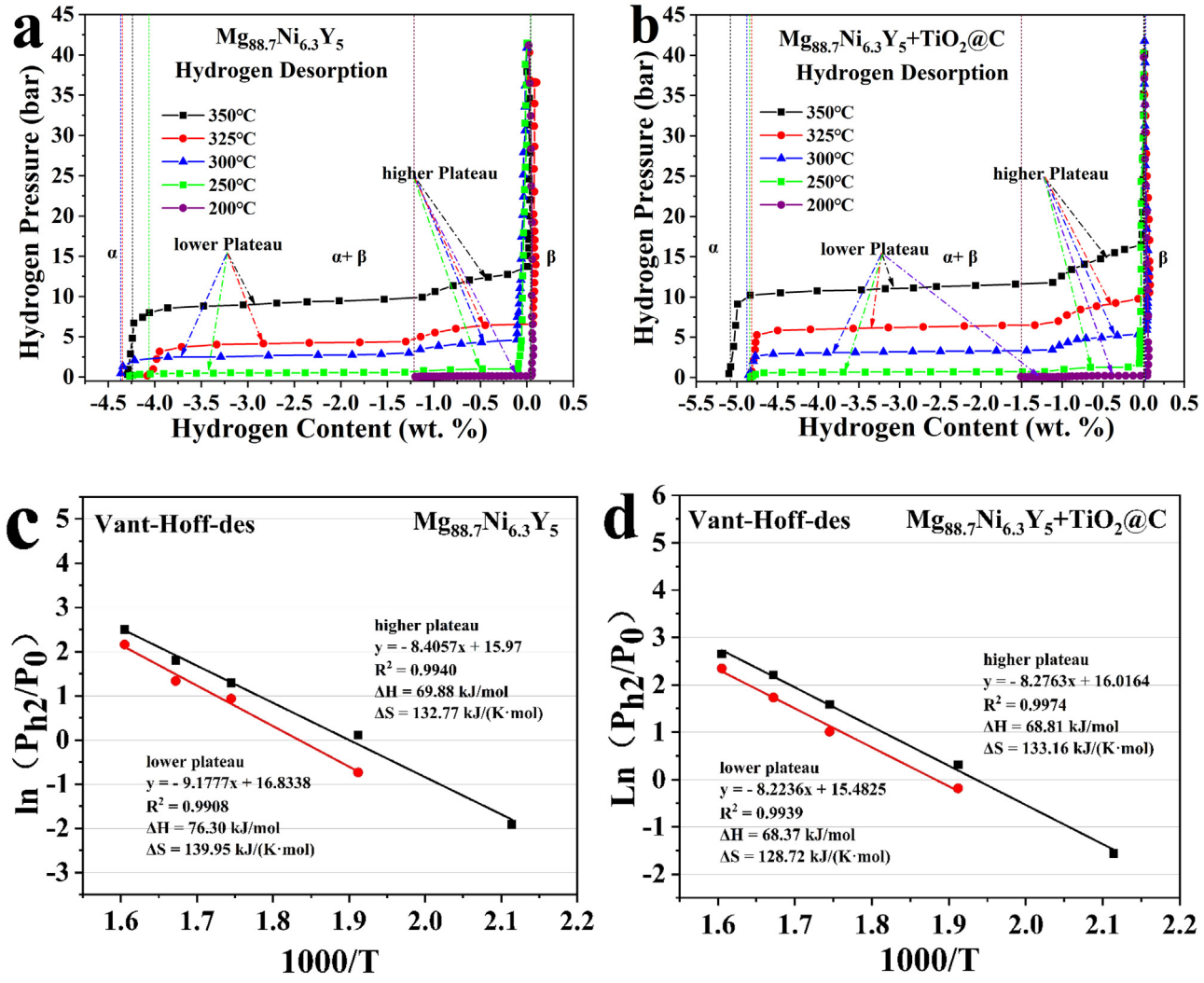

Fig. 8. Hydrogen desorption PCT and Vant Hoff curves. (a) PCT curves of $Mg_{88.7}Ni_{6.3}Y_5$; (b) PCT curves of $Mg_{88.7}Ni_{6.3}Y_5$+TiO_2@C; (c) $Mg_{88.7}Ni_{6.3}Y_5$ Vant Hoff desorption curves; (d) $Mg_{88.7}Ni_{6.3}Y_5$+TiO_2@C Vant Hoff desorption curves.

Table 1
$Mg_{88.7}Ni_{6.3}Y_5$ as-cast hydrogen desorption initial temperature and peak temperature.

Heating rates (K/min)	The First peak		The Second peak	
	Beginning dehydrogenation temperature(K)	The First peak dehydrogenation temperature(K)	Beginning dehydrogenation temperature(K)	The Second peak dehydrogenation temperature(K)
5	460.78	488.91	583.90	611.80
10	464.03	500.19	587.51	623.27
15	475.92	511.86	604.32	635.47
20	475.04	517.10	602.49	640.42

Table 2
$Mg_{88.7}Ni_{6.3}Y_5$+TiO_2@C hydrogen desorption initial temperature and peak temperature.

Heating rates (K/min)	The First peak		The Second peak	
	Beginning dehydrogenation temperature(K)	The First peak dehydrogenation temperature(K)	Beginning dehydrogenation temperature(K)	The Second peak dehydrogenation temperature(K)
5	464.90	499.87	576.27	607.33
10	476.80	516.95	584.58	633.35
15	487.19	527.57	593.75	646.17
20	513.16	535.35	590.98	654.05

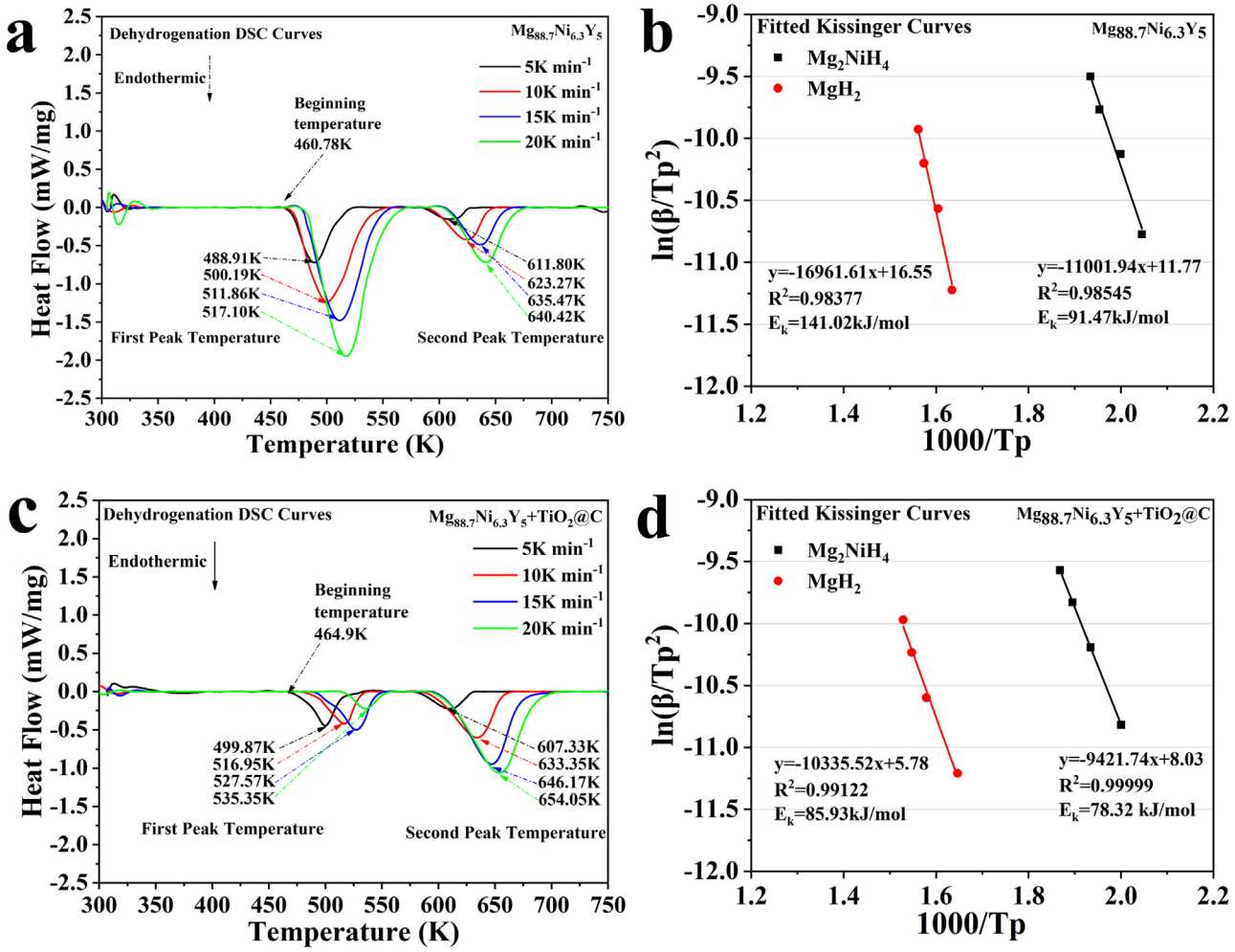

Fig. 9. DSC curves of $Mg_{88.7}Ni_{6.3}Y_5$ and $Mg_{88.7}Ni_{6.3}Y_5$+TiO_2@C hydrogenated alloy. (a) DSC curve of $Mg_{88.7}Ni_{6.3}Y_5$ alloy; (b) Kissinger curve of $Mg_{88.7}Ni_{6.3}Y_5$ alloy; (c) DSC curve of $Mg_{88.7}Ni_{6.3}Y_5$+TiO_2@C alloy; (d) Kissinger curve of $Mg_{88.7}Ni_{6.3}Y_5$+TiO_2@C alloy.

tivated TiO_2@C, the hydrogen molecule were dissociated into free hydrogen atoms. The multivalent titanium-based catalysts as electron carriers provide additional electrons for the chemical reaction between Mg^{2+} and H^- to promote the formation of Mg-H bonds. Pan et al. [36] studied that high valence Ti-based catalyst decompose into lower-valent species and even zero-valent metal, which in-situ created multivalent multielement catalytic surroundings. The H atoms were thus transferred through the "hydrogen overflow'' effect of TiO_2. The mobility of hydrogen atoms is much higher when close to adjacent Ti monomers than when close to TiO_2 [37], so Ti can react with hydrogen to form low valence Ti-based hydrides [38]. Li et al. [39] found that the content of TiO_2 catalyst was partially reduced after the first hydrogenation and dehydrogenation cycles. The conversion of multiple valence Ti-compounds was also accompanied by the formation of MgO. Some studies concluded that small additions of MgO were more effective in improving the kinetics of Mg-based hydrogen storage materials than other types of oxides [40,41], but the hydrogen storage capacity of the material decreased with the formation of excessive amounts of MgO [42]. Pukazhselvan [43] suggested that the Ti doped into the MgO phase formed a single oxide rock salt phase of MgO/TiO mixtures. Unlike the pure MgO layer, the rock salt phase was not the barrier layer which blocks the hydrogen diffusion path in the MgH_2 system.

Fig. 10(a) shows the schematic processes of the hydrogen absorption and desorption mechanisms of the TiO_2@C catalyzed $Mg_{88.7}Ni_{6.3}Y_5$ alloy with LPSO and ternary eutectic structure. There were abundant phase interfaces between the needle-shaped Mg_2Ni, Mg, $Mg_{15}NiY$ phases and the coarse Mg matrix in the ternary eutectic region. Faster diffusion of hydrogen atoms took place at the phase boundaries compared to that in the interior of the matrix. The freely-formed boundaries among the various phases in the ternary eutectic microstructure during solidification possessed a large contact area with each other. The multiphase structure should exhibit catalytic and synergistic effects on the hydrogen absorption and desorption. High-energy ball milling reduced the size of the particles to the nanoscale, shortening the diffusion distances of hydrogen atoms and contributing to the improvement of kinetics. Cui et al. [44] prepared multiphase

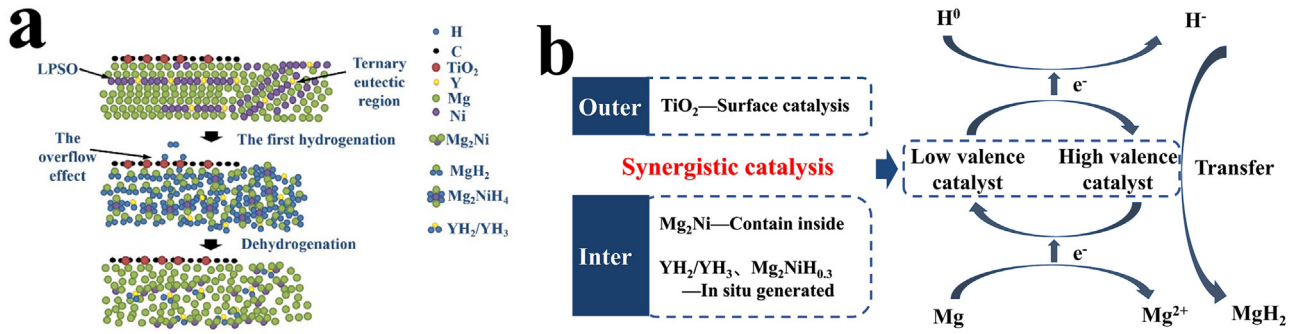

Fig. 10. (a) Schematic diagram of catalyst hydrogen absorption mechanism of $Mg_{88.7}Ni_{6.3}Y_5$ alloy catalyzed with TiO_2@C; (b) electron transfer during hydrogen absorption and desorption.

multivalent Ti-based nanocatalysts with a core-shell structure, demonstrating that multivalent Ti-based catalysts can provide a large number of active centres for electron transfer and valence conversion. During hydrogen absorption, H_2 were dissociated into free state H^0 on the surface of the catalyst. On the surface of the catalyst and the alloy, Ti^{2+} lost electrons to form $Ti^{3+/4+}$, and H^0 gains electrons and converted to H^-. The $Ti^{3+/4+}$ ions accepted electrons from Mg to form Ti^{2+}; meanwhile, Mg lost electrons to form Mg^{2+}, and the Mg-H bond was formed by Mg^{2+} and H^- [45]. Zhang et al. [46] found that the nanostructured Mg_2Ni, YH_2/YH_3 had an improved effect on the hydrogen absorption and desorption performance of Mg-based hydrogen storage materials. In this work, there are externally added TiO_2@C and *in-situ* endogenous YH_2/YH_3, Mg_2Ni catalysts. The synergistic catalytic mechanism and electron transfer schematic drawing are shown in Fig 10(b).

The LPSO structure was decomposed into MgH_2, $Mg_2NiH_{0.3}$, Mg_2NiH_4 and YH_2/YH_3 phases. The intermediate phases $Mg_2NiH_{0.3}$ and YH_2 in the hydrogen absorption and desorption process played an important role in the diffusion of H atoms to Mg 21,47–50]. The intermediate phase $Mg_2NiH_{0.3}$ and YH_2 could act as catalysis of MgH_2 by weakening the Mg-H bond, reducing the reaction energy barrier between Mg and H, and participating in the nucleation of MgH_2 as carriers of H atoms and a large number of free electrons. The intermediate phases $Mg_2NiH_{0.3}$ and YH_2 transform to Mg_2NiH_4 and YH_3 after complete hydrogenation. In the dehydrogenation process, Mg_2NiH_4 dehydrogenates to $Mg_2NiH_{0.3}$ first, then MgH_2 dehydrogenates. The H atoms transfer outward through the catalytic phases $Mg_2NiH_{0.3}$, YH_3 and a large number of grain/phase boundaries. Mg phase begins to nucleate, and then YH_3, $Mg_2NiH_{0.3}$ are dehydrogenated to YH_2, Mg_2Ni.

The improved hydrogen absorption kinetics and hydrogen storage capacity of the samples were attributed to the nanocatalysts loaded on the low-dimensional carbon materials as "hydrogen pumps''. This accelerated the dissociation of hydrogen which diffused into the alloy 45,51–53]. The fine catalysts for the decomposition of LPSO structure after hydrogen absorption were evenly distributed within the alloy, providing rich interphase boundaries. The nucleation of hydride at these boundaries shortened the diffusion distances of hydrogen [54,55] and mitigated the adverse effect of the hydrogenation layer on the diffusion of hydrogen atoms. The multiphase eutectic microstructure, *in-situ* formed nano-catalytic phase and added catalyst TiO_2@C synergistically improved the hydrogen storage properties.

4. Summary and concluding remarks

Based on the experimental results and analyses, the following conclusions can be drawn from this work.

The maximum hydrogen storage capacity of ball-milled as-cast $Mg_{88.7}Ni_{6.3}Y_5$ alloy catalyzed with TiO_2@C catalyst is 5.32 wt.%. Catalyzed alloy absorbed 4.25 wt.% H_2 in 1 min at 200 °C and 30 bar and demonstrated decent hydrogen desorption performance at 200 °C. The TiO_2@C catalyst improved the thorough hydrogen absorption and desorption reactions of MgH_2. The multiphase eutectic structure with alternating fine phases in the $Mg_{88.7}Ni_{6.3}Y_5$ alloy provides abundant interphase boundaries and active sites for hydrogen diffusion and the nucleation and growth of hydrides. The nano-TiO_2@C was uniformly distributed on the surface of the nanometer $Mg_{88.7}Ni_{6.3}Y_5$ alloy, which helped to prevent the agglomeration of the nanoscale alloy particles and improved the catalytic efficiency. The external TiO_2@C catalyst and the *in-situ* endogenous catalyst from the decomposition of the LPSO structure and ternary eutectic structure synergistically improved the hydrogen storage performance of $Mg_{88.7}Ni_{6.3}Y_5$ alloy.

Declaration of competing interest

The authors declare that they have no known competing financial interests or personal relationships that could have appeared to influence the work reported in this paper.

Acknowledgments

This work was partially supported by the National Key R&D Program of China (No. 2020YFA0406204), the National Natural Science Foundation of China (No. 52201265), Shaanxi Province Key Project of Research and Development Plan, China (No. 2023-YBGY-294, No. 2023KXJ-060) and the Doctoral Scientific Research Starting Foundation of

Shaanxi University of Science and Technology, China (No. 2016GBJ-02).

References

[1] L. Schlapbach, A. Zuttel, Nature 414 (2001) 353–358.
[2] X.B. Yu, Z.W. Tang, D.L. Sun, L.Z. Ouyang, M. Zhu, Prog. Mater Sci. 88 (2017) 1–48.
[3] L.Z. Ouyang, F. Liu, H. Wang, J.W. Liu, X.S. Yang, L.X. Sun, M. Zhu, J. Alloy Compd. 832 (2020) 154865.
[4] J.F. Song, J. She, D.L. Chen, F.S. Pan, J. Magnes Alloy 8 (2020) 1–41.
[5] J.G. Zhang, Y.F. Zhu, L.L. Yao, C. Xu, Y.N. Liu, L.Q. Li, J. Alloy Compd. 782 (2019) 796–823.
[6] Q. Luo, J.D. Li, B. Li, B. Liu, H.Y. Shao, Q. Li, J. Magnes Alloy 7 (2019) 58–71.
[7] F. Guo, T. Zhang, L. Shi, L. Song, Int. J. Hydrogen Energ. 45 (2020) 32221–32233.
[8] S. Kalinichenka, L. Röntzsch, T. Riedl, T. Weißgärber, B. Kieback, Int. J. Hydrogen Energ. 36 (2011) 10808–10815.
[9] F. Marques, H.C. Pinto, S.J.A. Figueroa, F. Winkelmann, M. Felderhoff, W.J. Botta, G. Zepon, Int. J. Hydrogen Energ. 45 (2020) 19539–19552.
[10] H.X. Huang, J.G. Yuan, B. Zhang, J.G. Zhang, Y.F. Zhu, L.Q. Li, Y. Wu, J. Alloy Compd. 839 (2020) 155387.
[11] C. Lu, Y. Ma, F. Li, H. Zhu, X. Zeng, W. Ding, T. Deng, J. Wu, J. Zou, J. Mater. Chem. A 7 (2019) 14629–14637.
[12] S. Liu, J. Liu, X. Liu, J. Shang, L. Xu, R. Yu, J. Shui, Nat. Nanotechnol. 16 (2021) 331–336.
[13] W. Song, H. Dong, G. Zhang, J. Liu, G. Yang, Y. Liu, Y. Li, J. Li, J. Shen, Y. Chen, Q. Wei, J. Alloy Compd. 820 (2020) 153187.
[14] Y. Sun, D.B. Wang, J.M. Wang, B.Z. Liu, Q.M. Peng, Int. J. Hydrogen Energ. 44 (2019) 23179–23187.
[15] H.C. Zhong, Y.S. Huang, Z.Y. Du, H.J. Lin, X.J. Lu, C.Y. Cao, J.H. Chen, L.Y. Dai, Int. J. Hydrogen Energ. 45 (2020) 27404–27412.
[16] H. Yong, X. Wei, J.F. Hu, Z.M. Yuan, S.H. Guo, D.L. Zhao, Y.H. Zhang, J. Magnes. Alloy 9 (2021) 1977–1988.
[17] H. Yong, S.H. Guo, Z.M. Yuan, W. Zhang, Y. Qi, D.L. Zhao, Y.H. Zhang, J. Rare Earth 38 (2020) 633–641.
[18] X. Pang, L. Ran, Y.A. Chen, Y. Luo, F. Pan, J. Magnes. Alloy 10 (2022) 821–835.
[19] J.Q. Du, Z.Q. Lan, H. Zhang, S.X. Lu, H.Z. Liu, J. Guo, J. Alloy Compd. 802 (2019) 660–667.
[20] Z.L. Ma, J.C. Liu, Y.F. Zhu, Y.Y. Zhao, H.J. Lin, Y. Zhang, H.W. Li, J.G. Zhang, Y.N. Liu, W.T. Gao, S.S. Li, L.Q. Li, J. Alloy Compd. 822 (2020) 153553.
[21] M. Chen, Y.Q. Wang, X.Z. Xiao, Y.H. Lu, M. Zhang, J.G. Zheng, L.X. Chen, Appl. Surf. Sci. 541 (2021) 148375.
[22] Z. Han, Y. Wu, H. Yu, S. Zhou, J. Magnes. Alloy 10 (2022) 1617–1630.
[23] D.C. Feng, D.S. Zhou, Z.Y. Zhao, T.T. Zhai, Z.M. Yuan, H. Sun, H.P. Ren, Y.H. Zhang, Int. J. Hydrogen Energ. 46 (2021) 33468–33485.
[24] Q.Y. Zhang, Y.K. Huang, T.C. Ma, K. Li, F. Ye, X.C. Wang, L.F. Jiao, H.T. Yuan, Y.J. Wang, J. Alloy Compd. 825 (2020) 153953.
[25] B. Li, B. Xi, F. Wu, H. Mao, J. Liu, J. Feng, S. Xiong, Adv. Engery Mater. 9 (2019) 1803070.
[26] J.W. Liu, C.C. Zou, H. Wang, L.Z. Ouyang, M. Zhu, Int. J. Hydrogen Energ. 38 (2013) 10438–10445.
[27] M. Mezbahul-Islam, D. Kevorkov, M. Medraj, Metals (Basel) 5 (2015) 1746–1769.
[28] X.Q. Tran, S.D. Mcdonald, Q.F. Gu, T. Yamamoto, K. Shigematsu, K. Aso, E. Tanaka, S. Matsumura, K. Nogita, J. Power Sources 341 (2017) 130–138.
[29] D.K. Yadav, K. Chawla, N Lal Pooja, B.L. Choudhary, C. Lal, Mater. Today-Proc. 46 (2021) 2326–2329.
[30] M. Zhang, X.Z. Xiao, B.S. Luo, M.J. Liu, M. Chen, L.X. Chen, J. Energy Chem. 46 (2020) 191–198.
[31] K.C. Xian, B. Nie, Z.G. Li, M.X. Gao, Z.L. Li, C.X. Shang, Y.F. Liu, Z.X. Guo, H.G. Pan, Chem. Eng. J. 407 (2021) 127156.
[32] Y.C. Pan, J.X. Zou, X.Q. Zeng, W.J. Ding, T Nonferr. Metal. Soc. 24 (2014) 3834–3839.
[33] M. Chen, X.Z. Xiao, M. Zhang, J.F. Mao, J.G. Zheng, M.J. Liu, X.C. Wang, L.X. Chen, Mater. Today Energy 16 (2020) 100411.
[34] X. Zhang, Z.H. Leng, M.X. Gao, J.J. Hu, F. Du, J.H. Yao, H.G. Pan, Y.F. Liu, J. Power Sources 398 (2018) 183–192.
[35] H.Y. Tien, M. Tanniru, C.Y. Wu, F. Ebrahimi, Scripta Mater. 62 (2010) 274–277.
[36] L. Zhang, K. Wang, Y. Liu, X. Zhang, J. Hu, M. Gao, H. Pan, Nano Res. 14 (2020) 148–156.
[37] R. Vujasin, J. Grbović Novaković, N. Novaković, S. Giusepponi, M. Celino, J. Alloy Compd. 696 (2017) 548–559.
[38] M. Calizzi, D. Chericoni, L.H. Jepsen, T.R. Jensen, L. Pasquini, Int. J. Hydrogen Energ. 41 (2016) 14447–14454.
[39] G. Liu, L. Wang, Y. Hu, C. Sun, H. Leng, Q. Li, C. Wu, J. Alloy Compd. 881 (2021).
[40] I.E. Castelli, S.G. Soriga, I.C. Man, J. Chem. Phys. 149 (2018) 034704.
[41] J.-.R. Ares-Fernández, K.-.F. Aguey-Zinsou, Catalysts 2 (2012) 330–343.
[42] J. Zhang, H. Liu, P. Sun, C. Zhou, X. Guo, Z. Fang, J. Alloy Compd. 934 (2023) 167757.
[43] D. Pukazhselvan, N. Nasani, P. Correia, E. Carbo-Argibay, G. Otero-Irurueta, D.G. Stroppa, D.P. Fagg, J. Power Sources 362 (2017) 174–183.
[44] J. Cui, J. Liu, H. Wang, L. Ouyang, D. Sun, M. Zhu, X. Yao, J. Mater. Chem. A 2 (2014) 9645–9655.
[45] J. Cui, H. Wang, J.W. Liu, L.Z. Ouyang, Q.A. Zhang, D.L. Sun, X.D. Yao, M. Zhu, J. Mater. Chem. A 1 (2013) 5603–5611.
[46] Z.W. Wu, Y.T. Li, Q.A. Zhang, J. Alloy Compd. 685 (2016) 639–646.
[47] K. Xu, S.H. Liu, D.D. Huang, Y. Du, J. Mater. Sci. 53 (2018) 9243–9257.
[48] R. Chen, X. Ding, X. Chen, X. Li, Y. Su, J. Guo, H. Ding, H. Fu, Int. J. Hydrogen Energ. 44 (2019) 21999–22010.
[49] J. Zhang, Y. Yao, L. He, X.J. Zhou, L.P. Yu, X.Z. Lu, P. Peng, Energy 217 (2021) 119315.
[50] Y. Zhang, X. Wei, W. Zhang, Z. Yuan, J. Gao, H. Ren, J. Magnes. Alloy 9 (2021) 2063–2077.
[51] N.S. Norberg, T.S. Arthur, S.J. Fredrick, A.L. Prieto, J. Am. Chem. Soc. 133 (2011) 10679–10681.
[52] X.L. Zhang, Y.F. Liu, X. Zhang, J.J. Hu, M.X. Gao, H.G. Pan, Mater. Today Nano 9 (2020) 100064.
[53] L.T. Zhang, X.Z. Xiao, C.C. Xu, J.G. Zheng, X.L. Fan, J. Shao, S.Q. Li, H.W. Ge, Q.D. Wang, L.X. Chen, J. Phys. Chem. C 119 (2015) 8554–8562.
[54] Q. Li, Q. Luo, Q.-.F. Gu, J. Mater. Chem. A 5 (2017) 3848–3864.
[55] J. Čermák, L. Král, Acta Mater. 56 (2008) 2677–2686.